ADVANCED MATERIALS
www.advmat.de

Nickel Hydroxide Catalyzed Bias-free Photoelectrochemical NH_3 Production via Nitrate Reduction

Wonjoo Jin, Hyunju Go, Juyeon Jeong, Jeonghwan Park, Ahmad Tayyebi, Je Min Yu, Seungchul Kim, Keunsu Choi, Ji-Wook Jang,* and Kwanyong Seo**

The photoelectrochemical nitrate reduction reaction (PEC NO_3RR) potentially converts nitrate, a major water pollutant, into NH_3, which is an eco-friendly, next-generation energy source. However, achieving high efficiency in the PEC NO_3RR has been challenging because of the need for high applied voltage and competition with the hydrogen evolution reaction (HER). In this study, a PEC NO_3RR is successfully implemented that demonstrated a high NH_3 production rate of 2468 µg cm^{-2} h^{-1} (at −0.1 V vs RHE) using a *c*-Si photocathode with Ni foil as the catalyst. Conducting the PEC NO_3RR under alkaline conditions can lead to the self-activation of the Ni surface with $Ni(OH)_2$. $Ni(OH)_2$ can suppress the competitive HER and facilitate NO_3RR, enhancing NH_3 production efficiency. Furthermore, a PEC NO_3RR system is developed that operates without external voltage and achieved bias-free record-high solar to NH_3 conversion efficiency of 3.8% and an NH_3 production rate of 554 µg cm^{-2} h^{-1}.

1. Introduction

Ammonia (NH_3), an essential chemical widely used in industry and agriculture, has an annual production exceeding 150 million tons.[1,2] NH_3 is a promising next-generation energy source for hydrogen transportation owing to its low explosion risk, ease of storage and transportation, safety, and high hydrogen content (17.6%).[2–4] Therefore, NH_3 is considered the most viable hydrogen carrier from economic and environmental perspectives.[5] However, most current NH_3 production relies on the Haber–Bosch process, which requires substantial energy inputs at high temperatures and pressures (400 °C and 200 bar).[6] This contributes to CO_2 emissions, accounting for 1.4% of global emissions and 1% of global energy consumption.[7] Consequently, developing environmentally friendly NH_3 production methods as alternatives to the Haber–Bosch process is urgently required.[8]

Electrochemical conversion is a promising method for eco-friendly NH_3 synthesis, potentially replacing the Haber–Bosch process. However, the electrochemical nitrogen reduction reaction (N_2RR) for NH_3 synthesis has been challenging as an alternative because of the high dissociation energy (945 kJ mol^{-1}) of the N≡N bond and its low water solubility (1.17×10^{-5} mol at 25 °C, 1 atm N_2).[2] Furthermore, the substantial energy required to break the nitrogen triple bond contributes to a low efficiency of NH_3 production.[9] In contrast, nitrate anions (NO_3^-) are an ideal candidate for electrochemical NH_3 synthesis with their relatively low dissociation energy (204 kJ mol^{-1}) of the N = O bond and high solubility (3.79 mol at 25 °C).[10] Additionally, nitrates, commonly found in industrial wastewater at ≈0.8 mM to 2 M concentrations, pose environmental and health risks by contributing to soil eutrophication, blue baby syndrome, and gastrointestinal cancers.[11–13] Therefore, the electrochemical conversion of nitrate to NH_3 (nitrate reduction reaction, NO_3RR) facilitates the production of next-generation energy sources as well as offers a synergistic approach to water treatment, providing significant environmental and health benefits.

W. Jin, H. Go, J. Jeong, J. Park, A. Tayyebi, J. M. Yu, J.-W. Jang, K. Seo
School of Energy and Chemical Engineering
Ulsan National Institute of Science and Technology (UNIST)
Ulsan 44919, Republic of Korea
E-mail: jiwjang@unist.ac.kr; kseo@unist.ac.kr

S. Kim
Computational Science Research Center
Korea Institute of Science and Technology (KIST)
Seoul 02792, Republic of Korea

K. Choi
Department of Physics
Ulsan National Institute of Science and Technology (UNIST)
Ulsan 44919, Republic of Korea
E-mail: ubercgs@unist.ac.kr

J.-W. Jang
Emergent Hydrogen Technology R&D Center
Ulsan National Institute of Science and Technology (UNIST)
Ulsan 44919, Republic of Korea

J.-W. Jang, K. Seo
Graduate School of Carbon Neutrality
Ulsan National Institute of Science and Technology (UNIST)
Ulsan 44919, Republic of Korea

The ORCID identification number(s) for the author(s) of this article can be found under https://doi.org/10.1002/adma.202506567

DOI: 10.1002/adma.202506567

The electrochemical NO_3RR can be expressed by the following half-reaction Equation (1): [14]

$$NO_3^- + 6\,H_2O + 8\,e^- \rightarrow NH_3 + 9\,OH^-\ E^\circ = 0.69 V_{RHE} \quad (1)$$

The photoelectrochemical nitrate reduction reaction (PEC NO_3RR), which derives the electric potential required for the reaction through the photovoltaic process, converts nitrate into NH_3 in a more environmentally sustainable manner. Consequently, research on the PEC NO_3RR has received significant attention.[2,15–17] Kim et al. reported that by depositing Au as a cocatalyst on silicon nanowire (SiNW) to form SiNW/Au, they facilitated the rate-determining step of the NO_3RR: the conversion of NO_3^- to NO_2^-.[2] This approach resulted in a low NH_3 production rate of 7.07 μg cm^{-2} h^{-1} (at 0.1 V vs RHE). Wang et al. used a $ZnIn_2S_4/BiVO_4$ heterostructure catalyst, known for its high photoelectrochemical performance owing to its small band gap, to leverage Frustrated Lewis pairs to enhance selective chemisorption and catalytic kinetics. They achieved an NH_3 production rate of 29.95 μg cm^{-2} h^{-1} (at −0.1 V vs RHE).[15] Ren et al. reported an NH_3 production rate of 270.96 μg cm^{-2} h^{-1} (at −0.2 V vs RHE) with a Faradaic efficiency of 88.01% using a $CoCu/TiO_2/Sb_2Se_3$ photocathode.[16] Ding et al. demonstrated the first bias-free solar-to-NH_3 production using a Cu/C/Si-TiO_2 tandem photoelectrode, achieving an NH_3 production rate of 223.10 μg cm^{-2} h^{-1} and solar-to-NH_3 conversion (STA) efficiency of 1.5%.[17] However, considering the very low NH_3 production rate and low efficiency of solar-to-NH_3 conversion, conducting research that significantly enhances these efficiencies is essential. However, challenges have been encountered with respect to the stability of NH_3 production, primarily resulting from detachment or corrosion of nitrate reduction electrocatalysts.

In this study, crystalline silicon (*c*-Si) was employed as the photoelectrode material for the PEC NO_3RR, with a nickel (Ni) foil serving as an encapsulation layer for *c*-Si from the electrolyte as well as a nitrate reduction electrocatalyst. *c*-Si is a highly favorable material for PEC because of its abundance on Earth, high carrier mobility, and relatively optimal bandgap of 1.1 eV.[18] In alkaline conditions, Ni naturally forms Ni hydroxide ($Ni(OH)_2$) due to thermodynamically favorable oxidation.[19] Experimental and theoretical evidence demonstrate that self-activated $Ni(OH)_2$ under alkaline conditions can accelerate the NO_3RR by effectively suppressing the competing hydrogen evolution reaction (HER). Furthermore, owing to the direct conversion of the Ni foil surface to $Ni(OH)_2$, the robust interaction between $Ni(OH)_2$ and the Ni foil inhibits the detachment of $Ni(OH)_2$ from the Ni foil, unlike in post-deposited nitrate reduction electrocatalysts (SiNW/Au).[2] Additionally, $Ni(OH)_2$ electrocatalysts have no corrosive issues, which are critical challenges for Cu-based nitrate reduction electrocatalysts.[16,17] Consequently, a *c*-Si photocathode equipped with $Ni(OH)_2$@Ni foil as the catalyst achieved an NH_3 production rate of 2468 μg cm^{-2} h^{-1} (at −0.1 V vs RHE), the highest value reported with no evidence of performance decrease over five cycles of stability testing. Furthermore, this study implemented a *c*-Si all-back contact (ABC) photocathode, enabling bias-free solar to NH_3 conversion directly by sunlight. It attained an NH_3 production rate of 554 μg cm^{-2} h^{-1} and an STA of 3.8%, representing the highest efficiency achieved to date for bias-free NH_3 production via PEC NO_3RR.

2. Results and Discussion

2.1. Nitrate Reduction Reaction Using *c*-Si Photocathode

The PEC NO_3RR using a *c*-Si photocathode is illustrated in **Figure 1a**. The *c*-Si photocathode comprised a *c*-Si *p-n* junction for light absorption and efficient carrier separation and a Ni foil as the catalyst. After light absorption, the *c*-Si photocathode generated photoinduced electrons, leading to a nitrate reduction reaction. At the *c*-Si/electrolyte junction, *c*-Si formed a direct heterojunction with the electrolyte, resulting in a relatively low photovoltage (≈0.2 V).[20,21] Recently, research has focused on forming a *p-n* junction in *c*-Si through doping to address this issue, resulting in high efficiency.[22–25] Utilizing the *c*-Si *p-n* junction resulted in a relatively high photovoltage (≈0.6 V), which is attributed to the energy difference between the quasi-Fermi levels formed through Fermi-level splitting under light illumination. Compared to the *c*-Si/electrolyte heterojunction, where the photovoltage is relatively low, the *p-n* junction structure enables the formation of a higher photovoltage, leading to a more efficient photoelectrochemical reaction (Figure S1, Supporting Information).[25–30] To evaluate the PEC NO_3RR performance of *c*-Si/electrolyte junction photocathodes in comparison with *c*-Si *p-n* junction photocathodes, linear sweep voltammetry (LSV) curves were obtained using three-electrode measurements under AM 1.5G illumination (1 sun, 100 mW cm^{-2}). As shown in Figure 1b, compared to the onset potential of the conventional *c*-Si/electrolyte junction photocathode (−0.09 V, −1 mA cm^{-2}), the *c*-Si *p-n* junction photocathode exhibited a relatively positively shifted onset potential (0.69 V, −1 mA cm^{-2}). This shift toward a more positive potential was attributed to the open-circuit voltage of the *c*-Si *p-n* junction (Figure S2, Supporting Information). A significant distinction in the onset potential was further clarified through a 1 h chronoamperometry (CA) measurement (Figure 1c). At the same bias of −0.1 V versus RHE, the *c*-Si *p-n* junction photocathode maintained a stable current density of 37.5 mA cm^{-2} over 1 h. In contrast, the *c*-Si/electrolyte junction photocathode recorded a much lower value of 2.5 mA cm^{-2}. This suggests that the additional photovoltage from the *c*-Si *p-n* junction photocathode facilitated more efficient nitrate reduction. The observed current density for the *c*-Si *p-n* junction photocathode aligned well with the integrated external quantum efficiency value (Figure S3 and Note S1, Supporting Information).

Furthermore, a comparison between the *c*-Si photocathode with directly attached $Ni(OH)_2$ and the *c*-Si photocathode with self-activated $Ni(OH)_2$ on Ni foil reveals that the *c*-Si photocathode with self-activated $Ni(OH)_2$ exhibits high stability, while the *c*-Si photocathode with directly attached $Ni(OH)_2$ shows very low stability (Figure S4, Supporting Information). This observation indicates that the Ni foil not only serves as a catalyst but also functions as a passivation layer. Moreover, the Faradaic efficiency (FE) and produced NH_3 yield for the NO_3RR were quantified using the indophenol blue method (Figure S5, Supporting Information). According to Figure 1d, the FE for the *c*-Si/electrolyte junction and *c*-Si *p-n* junction photocathodes were ≈60% and 85%, respectively, with corresponding NH_3 yields of 195 and

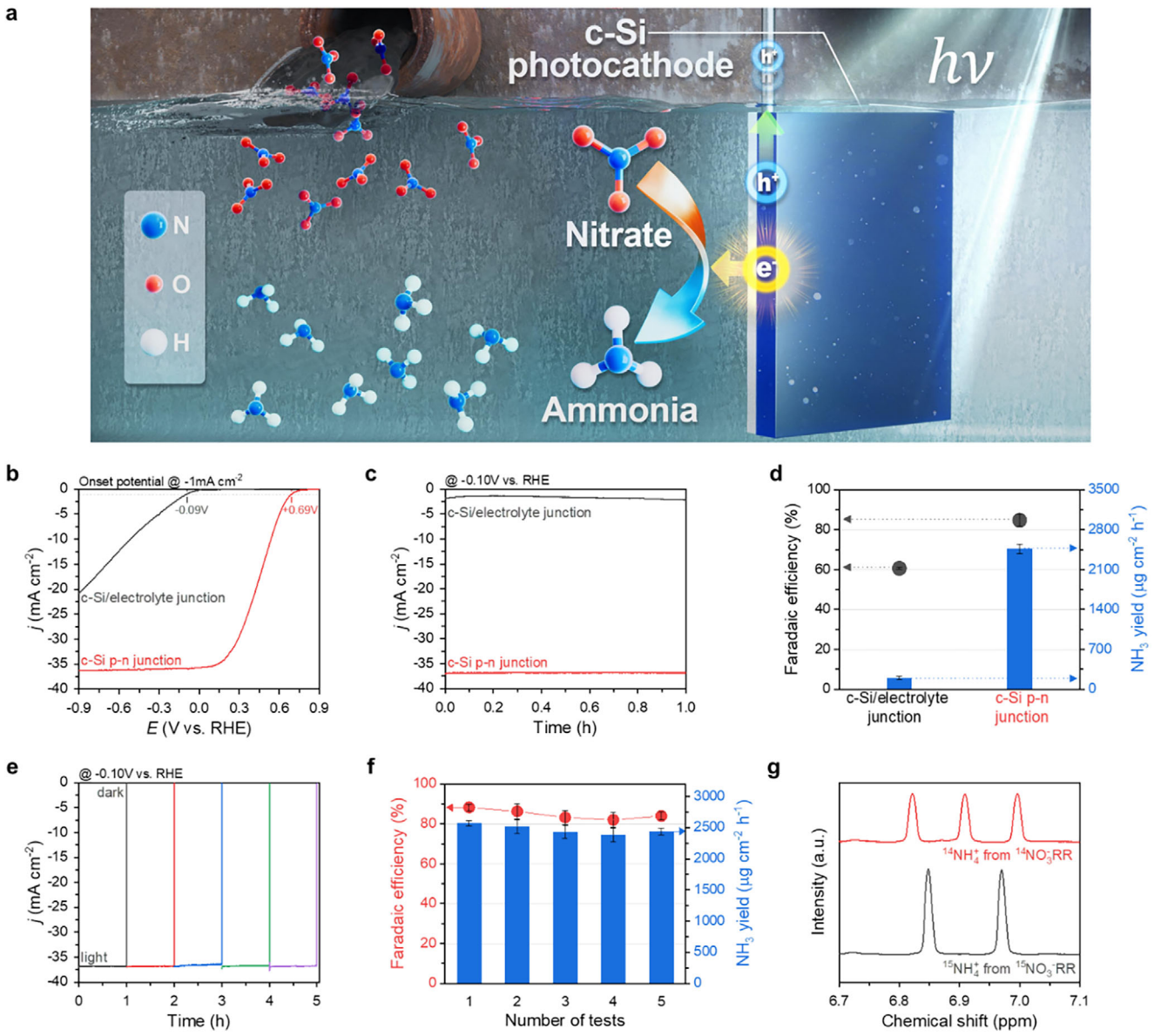

Figure 1. Photoelectrochemical nitrate reduction reaction using *c*-Si photocathode. a) Schematic illustration of the PEC NO_3RR. b) Linear sweep voltammetry (LSV) curves of *c*-Si/electrolyte junction (black line) and *c*-Si *p-n* junction (red line) photocathodes under simulated solar light irradiation (AM 1.5G). c) Chronoamperometry curves, and d) Faradaic efficiency and NH_3 yield rate of the *c*-Si/electrolyte junction (black) and *c*-Si *p-n* junction (red) photocathode at -0.1 V (vs RHE). e) Cycle stability and f) Faradaic efficiency and NH_3 yield rate of *c*-Si *p-n* junction photocathode measured by NO_3RR cycle performance at -0.1 V (vs RHE). g) ^{1}H-NMR spectra of electrolyte produced from NO_3RR under -0.1 V (vs RHE) using $K^{14}NO_3$ and $K^{15}NO_3$ as N source.

2468 μg cm^{-2} h^{-1}. These results indicate that, owing to the additional photovoltage, the *c*-Si *p-n* junction photocathode significantly surpasses the performance of the existing *c*-Si/electrolyte junction photocathode in terms of NH_3 production. To investigate the PEC performance stability of the *c*-Si *p-n* junction photocathode, a PEC NO_3RR cycle test was conducted at −0.1 V versus RHE. The chronoamperometry (CA) graph showed stable maintenance without a decrease in the photocurrent during the repeated cycle tests (Figure 1e). Additionally, a high FE, averaging 86%, and a high NH_3 production rate of 2500 μg cm^{-2} h^{-1} were confirmed (Figure 1f). To ensure that the NH_3 produced was the result of nitrate reduction rather than from the other external sources, isotope tracing experiments were conducted at −0.1 V versus RHE using $K^{15}NO_3$ at the same concentration to confirm the relevant ^{1}H-NMR spectroscopy (Figure 1g). In the ^{1}H-NMR spectrum of the PEC NO_3RR using $K^{14}NO_3$ as the reactant, typical triple peaks of $^{14}NH_4^+$ were observed, whereas in the PEC NO_3RR using $K^{15}NO_3$ as the reactant, only the characteristic double peaks of $^{15}NH_4^+$.[31–33] These results demonstrate that NH_3 was produced only through the PEC NO_3RR rather than through other external sources such as the atmosphere.

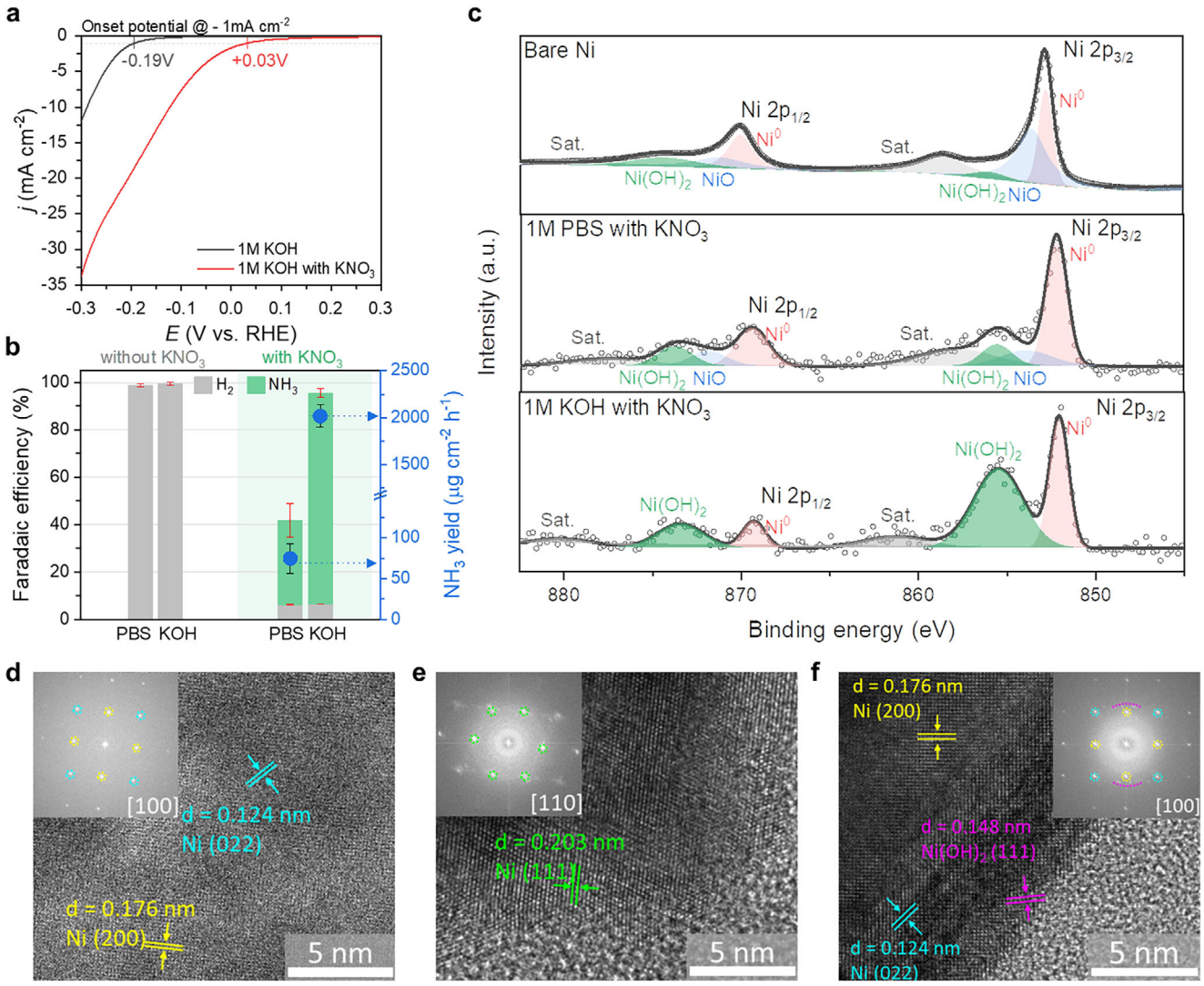

Figure 2. Ni electrocatalyst property. a) LSV curves of Ni foil in 1.0 M KOH electrolyte with (red line) and without (black line) 0.5 M KNO_3. b) Faradaic efficiency and NH_3 yield rate after NO_3RR in neutral and alkaline electrolytes. c) The analysis of X-ray photoelectron spectroscopy (XPS). High-resolution Ni 2p spectra of Ni foil before and after the NO_3RR in neutral and alkaline electrolytes High-resolution TEM (HRTEM) images d) Ni foil surface before experiment, and after experiment NO_3RR in e) neutral electrolyte and f) alkaline electrolyte with fast Fourier transform (FFT) patterns indicated by yellow dots for the Ni(200) peak, blue dots for Ni(022) peak, green dots for Ni(111) and pink dashed line for the $Ni(OH)_2$ (111) peak.

2.2. Ni Electrocatalyst Property

The Ni surface used as a catalyst can be self-activated to form $Ni(OH)_2$ through a reduction reaction.[19] To investigate how the catalytic properties of the Ni foil in the NO_3RR changed with the pH of the electrolyte, the NO_3RR performances were compared and analyzed at different pH levels. Ni leaches into acidic aqueous solutions.[34] Inductively coupled plasma optical emission spectroscopy (ICP-OES) was performed to verify the stability of the Ni foil under various pH conditions. Ni was not detected in the alkaline electrolyte, small amounts (0.386 ppm h^{-1}) of Ni were detected in the neutral electrolytes, and significant amounts (7.556 ppm h^{-1}) of Ni were detected in the acidic electrolytes (Figure S6, Supporting Information). Therefore, we conducted the NO_3RR only in neutral and alkaline electrolytes. The NO_3RR performance under neutral and alkaline electrolytes appears comparable in the LSV curves, but it is more pronounced under alkaline conditions (**Figures** 2a and S7, Supporting Information). As shown in Figure 2b, the device exhibits a FE of 35% and an NH_3 yield of 75 μg cm^{-2} h^{-1}, under neutral electrolyte conditions. In contrast, under alkaline conditions, the FE and NH_3 yield increased 89% and 2017 μg cm^{-2} h^{-1}, respectively. This indicates that the NO_3RR catalytic activity of the Ni foil was enhanced by more than 2.5 times in an alkaline electrolyte compared to that in a neutral electrolyte. This can be attributed to the self-activation of Ni to $Ni(OH)_2$, which occurs more readily in an alkaline electrolyte than in a neutral one.

To investigate the chemical state of the Ni surface before and after the NO_3RR under different pH conditions, we performed X-ray photoelectron spectroscopy (XPS) (Figure 2c). Before the reaction, the main peaks of Ni (Bare Ni) were observed at 852.9 and 870 eV for Ni $2p_{3/2}$ and Ni $2p_{1/2}$, respectively.[35] In contrast,

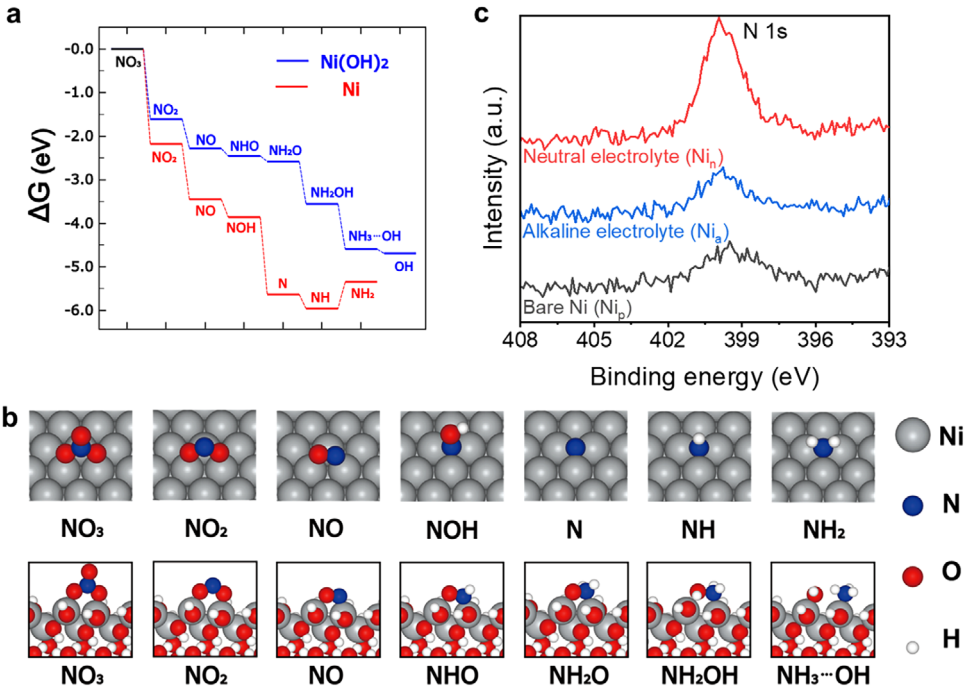

Figure 3. DFT calculation for nitrate reduction on Ni catalyst. a) Free energy diagram of the NO_3RR pathway on the Ni (red) and $Ni(OH)_2$ (blue). b) Optimized structures of the NO_3RR on the Ni (top) and $Ni(OH)_2$ (bottom). c) X-ray photoelectron spectroscopy (XPS) of pristine bare Ni foil (Ni_p, black) and Ni foils after completing the nitrate reduction reaction in neutral (Ni_n, red) and alkaline environments (Ni_a, blue).

after 1 h of NO_3RR, the Ni^{2+} peaks at 855.5 and 873.5 eV were observed in neutral and alkaline electrolytes, with a rapid increase particularly notable under alkaline conditions.[19,36] These XPS results indicated that the Ni surface was transformed into Ni^{2+} during the NO_3RR, with this transformation being significantly more dominant under alkaline conditions than under neutral conditions. For detailed analysis, after the NO_3RR under alkaline and neutral electrolyte conditions for 1 h, the Ni foil surface was examined using high-resolution transmission electron microscopy (HRTEM). Under alkaline electrolyte conditions, the HRTEM image confirmed the formation of $Ni(OH)_2$ on the Ni foil surface (Figure 2d–f). In addition, the fast Fourier transform (FFT) image (inset of Figure 2f) revealed the $Ni(OH)_2$ (111) crystal plane with a d-spacing of 0.148 nm.[37–41] However, in neutral electrolyte conditions, the $Ni(OH)_2$ structure was not observed on the Ni surface, and only the Ni(111) crystal plane was observed (Figure 2e).[39–41] These results further confirmed that the self-activation of Ni with $Ni(OH)_2$ was predominant under alkaline conditions. To enhance the efficiency of the NO_3RR, suppressing the HER, which is a competitive reaction, is essential. To investigate the NO_3RR activity of Ni, the performance of NO_3RR and HER of Ni as an electrocatalyst was compared under alkaline conditions. In the LSV curves in Figure 2a, the curves of the $Ni(OH)_2$@Ni catalyst were positively shifted for the NO_3RR compared to the HER, indicating that the NO_3RR is more dominant. Furthermore, as shown in Figure 2b, when the same voltage (−0.3 V vs RHE) is applied to induce the reduction reaction, the self-activated $Ni(OH)_2$ proves to be a more effective catalyst for NO_3RR than for HER. This is attributed to the fact that the H^* required for the NO_3RR is abundantly generated on the $Ni(OH)_2$@Ni surface, and this generated H^* catalyzes the reduction of nitrate more efficiently than H_2.[42] Therefore, the use of Ni foil as a catalyst for the NO_3RR is suitable.

2.3. Density Functional Theory (DFT) Calculation for Nitrate Reduction on Ni Catalyst

To elucidate the difference in the catalytic performance for the NO_3RR between Ni and $Ni(OH)_2$, we conducted DFT calculations. We calculated the free energies and the optimized structures for the multistep NO_3RR in both Ni and $Ni(OH)_2$, and the calculation results are provided in **Figure** 3a,b. Because Ni is a transition metal that binds the O atom strongly, we consider the adsorbed NO_3 as the initial reaction step, where NO_3 vertically binds to two Ni atoms on the Ni (111) and $Ni(OH)_2$ (101) surfaces. The adsorbed NO_3 is then successively reduced while the O atoms are exothermally desorbed in the form of H_2O by the supply of H from the surface of the catalysts. The optimized structures of the intermediates are equivalent in both catalysts up to the NO stage, where the N and O atoms form covalent bonds with the Ni atoms, respectively (Figure 3b). However, subsequent reduction reactions on the two surfaces follow different reaction paths. On the Ni surface, the adsorption of hydrogen on an oxygen atom induces the breaking of the Ni—O bond and the formation of three Ni-N covalent bonds. The OH bonded to the N atom is then desorbed into H_2O through the reduction reaction, and the subsequent reduction reactions add H to the remaining N atom. The reaction step ($NH \rightarrow NH_2$) exhibited an energy barrier (0.6 eV), indicating that further reduction reaction does not proceed and the N atom tends to remain on the Ni (111) surface in the form of NH. In contrary, all the successive reduction

reactions to the production of NH_3 exhibit exothermic reactions on the $Ni(OH)_2$ surface: NHO, NH_2O, NH_2OH, $NH_3\cdots OH$. In the NH_2OH step, the additional H adsorption to NH_2 induces the formation of NH_3 and the N—O bond breaking, where the N—O bond length increases from 1.47 to 2.58 Å. The N atom binds to only one Ni atom, and it makes NH_3 to be exothermally desorbed from the $Ni(OH)_2$ surface (Figure S8, Supporting Information). The desorption of the remaining OH from the $Ni(OH)_2$ surface to form H_2O is also an exothermic reduction reaction with a ΔG value of −0.09 eV. Therefore, the configurations of the surface Ni atoms originate the different reaction paths between Ni and $Ni(OH)_2$, resulting in different catalytic performance. Based on the computational results, we conducted XPS analysis on pristine bare Ni foils (Ni_p) and Ni foils after completing the nitrate reduction reaction in neutral (Ni_n) and alkaline environments (Ni_a). As shown in Figure 3c, the N content in Ni_n was significantly higher than that in Ni_p and Ni_a. The XPS results also indicated that the strong binding of the N atom to the Ni surface inhibited the reduction reaction, leading to fewer catalytic reactions.

2.4. Bias-Free PEC NH_3 Production

To achieve bias-free solar-to-NH_3 conversion solely using only solar energy without the need for an external voltage, a Ni/*c*-Si all-back contact (ABC) photocathode was employed. In conventional *c*-Si photoelectrodes, the electrocatalyst is positioned on the surface of the *c*-Si that is exposed to incident light, which reduces the overall photocurrent of the device. Recent innovations have introduced designs in which the electrocatalyst is positioned on the rear of the photoelectrode.[24,43] Specifically, the *c*-Si ABC photoelectrode employs a *p-n* junction and places all electrodes at the back side, thus eliminating concerns about light shading by the catalyst, meaning that the transparency of the catalyst is irrelevant. This strategy allows for greater flexibility in the selection of catalysts for photoelectrode design. In this study, we fabricated a photocathode using Ni foil as the electrocatalyst in combination with the *c*-Si ABC structure to reduce the overpotential of the NO_3RR. Detailed information on the fabrication process and structure of the *c*-Si ABC photocathode is provided in the Experimental section and Figure S9 (Supporting Information). **Figure 4a** shows a schematic of the bias-free solar to NH_3 conversion using a Ni/*c*-Si ABC photocathode and a NiFe-layered double hydroxide (LDH) anode. The *c*-Si ABC structure, serving as the photocathode, allowed the use of Ni foil as the electrocatalyst for the NO_3RR, enabling the predominant self-activation of $Ni(OH)_2$ without constraints related to the optical properties. For the counter-reaction to the NO_3RR, the oxygen evolution reaction (OER), NiFe-LDH, was selected as the anode material because of its exceptional effectiveness as an OER catalyst under alkaline conditions.[44,45] The synthesis method for NiFe-LDH is detailed in the Experimental section,[46] while the characteristics of the synthesized NiFe-LDH are shown in Figures S10 and S11 (Supporting Information).

Although NiFe-LDH is a premier OER catalyst, the LSV curves for the Ni/*c*-Si 1 cell ABC photocathode and NiFe-LDH, measured in a three-electrode configuration, did not intersect (Figure 4b). This indicates that a *c*-Si ABC unit cell alone is insufficient for generating an adequate photovoltage for bias-free solar to NH_3 production, necessitating an additional voltage. Consequently, to facilitate the bias-free solar-to-NH_3 conversion, an experiment was conducted in which the photovoltage of the Ni foil/*c*-Si ABC photocathode was increased by serially connecting multiple *c*-Si ABC unit cells (Figure S12, Supporting Information). When multiple *c*-Si *p-n* junction cells are connected in series, the total photovoltage increases proportionally to the number of connected cells, while the current density is determined by the current of a single cell in the series and is inversely proportional to the increased total area. The unique ABC configuration simplifies the interconnection between unit cells in module assembly, in contrast to conventional *c*-Si solar cell modules. This reduces the ohmic losses owing to the resistance of the interconnecting electrode and eliminates the need for extra space, thereby facilitating seamless module construction. Using a *c*-Si ABC 4 cell photocathode achieved optimal efficiency, with anticipated operating voltage and current density at 1.5 V (vs RHE), estimated to be 8.98 mA cm^{-2}, as evidenced by the overlaid LSV curves measured with the NiFe-LDH anode in a three-electrode setup (Figure 4b). The reliability of the bias-free solar-to-NH_3 conversion was confirmed through cycle testing in a two-electrode system. The integrated PEC system, comprising the Ni/*c*-Si ABC 4 cell photocathode and NiFe-LDH anode, operated stably at 8.7–8.8 mA cm^{-2} without photocurrent reduction across repeated cycle tests and external voltage (Figure 4c), closely aligning with the current density predictions from the LSV curve in the three-electrode configuration shown in Figure 4b. Consequently, the bias-free solar to NH_3 conversion using the Ni/*c*-Si ABC 4 cell photocathode maintained a stable FE of ≈80% across five cycles, as indicated in Figure 4d. The STA efficiency was calculated using the following Equation (2):

$$STA\,Efficiency\quad(\%) = \frac{(1.23V - 0.69V) \times J_{op}\left(mAcm^{-2}\right) \times FE\,(\%)}{100mWcm^{-2}} \times 100 \qquad (2)$$

The operating current density, J_{OP}, was determined from the intersection between the *J-V* characteristics and LSV curves of the 4 cell Si ABC photocathode and the NiFe-LDH anode. The difference of 1.23 and 0.69 V represents the standard reduction potentials for the total reactions of OER and NO_3RR in this system ($E^0_{NO3/NH3}$ = 0.69 V vs RHE, $E^0_{O2/H2O}$ = 1.23 V vs RHE). Consequently, the STA efficiency of the proposed system was 3.8% (Figure 4e). This represents a more than two-fold improvement over the previously reported bias-free PEC-based STA efficiency (1.5%).[17] For more accurate analysis, the NH_3 production rate of 554 μg cm^{-2} h^{-1} was confirmed again using the indophenol blue method, consistent with the calculated ≈3.8% STA efficiency (Figure 4e and Note S2, Supporting Information).

2.5. Scale-Up of the Ni/*c*-Si ABC Photocathode for the Bias-Free NO_3RR System

We have conducted scale-up tests to evaluate the feasibility of our bias-free NO_3RR system for commercial applications. Our system is inherently designed for scalability as it utilizes *c*-Si, which currently dominates more than 95% of the global

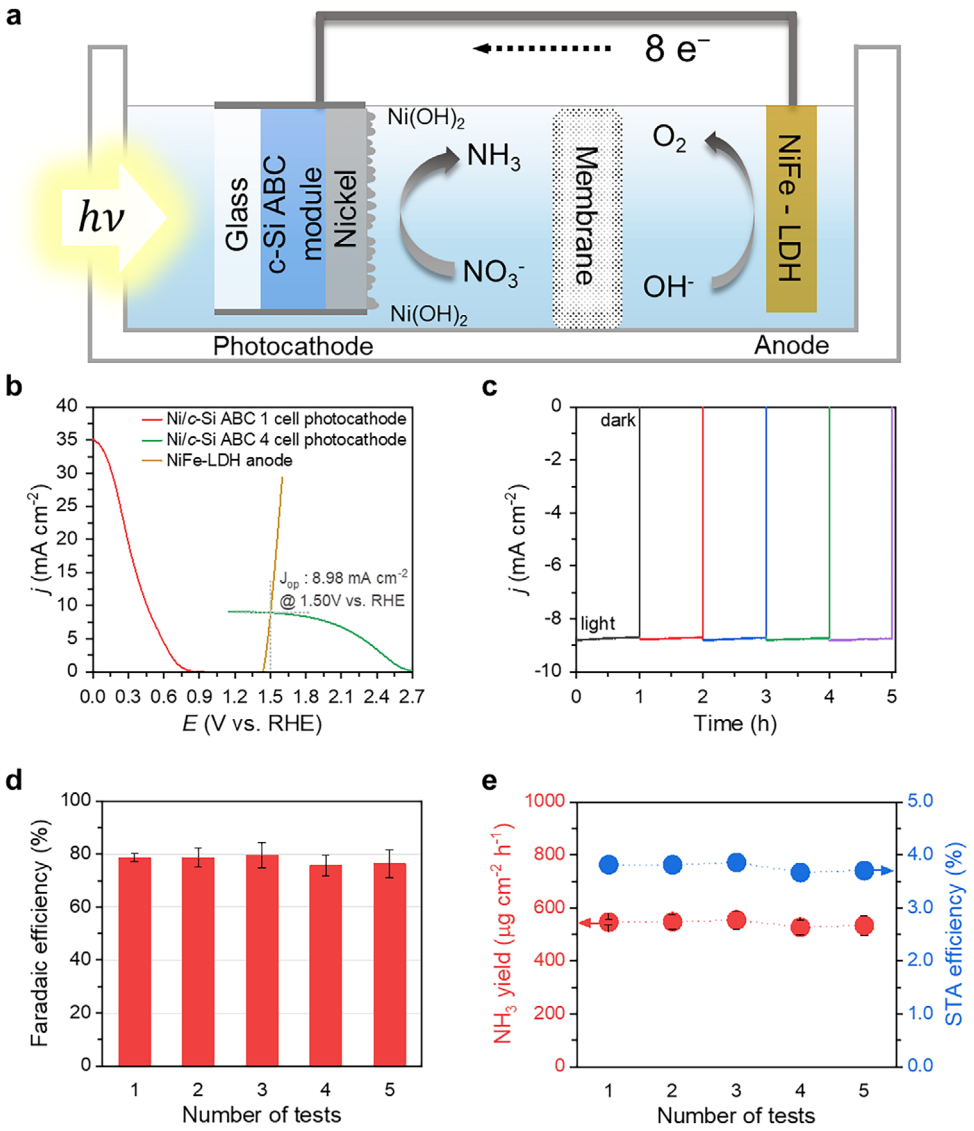

Figure 4. Overall, bias-free NH_3 production. a) Schematic of the overall reaction with the Ni/*c*-Si ABC photocathode and the NiFe-LDH anode. b) Overlap of the LSV curves of the Ni/*c*-Si ABC 1, 4 cell photocathode and NiFe-LDH anodes. c) Bias-free operating current in the integrated PEC system. d) Faradaic efficiency of the unassisted solar NH_3 production cycle performance. e) NH_3 production rate and STA efficiency for the PEC NO_3RR without external bias.

solar market due to its low cost, well-established manufacturing process, and high scalability.[47] As a widely commercialized photovoltaic material, *c*-Si ensures seamless integration into existing solar panel production lines, making our approach highly practical for large-scale deployment. To validate large-area operation, we tested a 25 cm^2 Ni/*c*-Si ABC 4-cell photocathode, as shown in **Figure** 5a. Compared to Figure 4b, the large-area photocathode demonstrated stable performance with no significant decline in the LSV curves, confirming that the scale-up process does not negatively impact the fundamental PEC characteristics (Figure 5b). Furthermore, the system maintained a constant photocurrent for 51 h without external bias, demonstrating excellent stability and durability (Figure 5c). In Figure 5d, we observed a gradual decrease in Faradaic efficiency over time, which we attribute to nitrate depletion rather than system degradation, such as catalyst or photocathode. Notably, the FE was fully restored upon replacing the electrolyte with a fresh nitrate source, further reinforcing the system's long-term operational stability. We also calculated a STA efficiency of 3.6%, confirming that scaling up the system does not lead to performance degradation. Notably, this efficiency remains comparable to the 3.8% STA efficiency reported in Figure 4e for the smaller-scale system, indicating that our PEC NO_3RR system maintains high performance even at increased scales. These results strongly support the practical and commercial potential of our approach while demonstrating its scalability without efficiency loss. To further highlight the significance of our results, we compared our system with existing PEC NO_3RR studies, demonstrating its performance under both biased and unbiased conditions.[2,16,17,48–57] As shown in Figure 5e and Table S1 (Supporting Information), our system

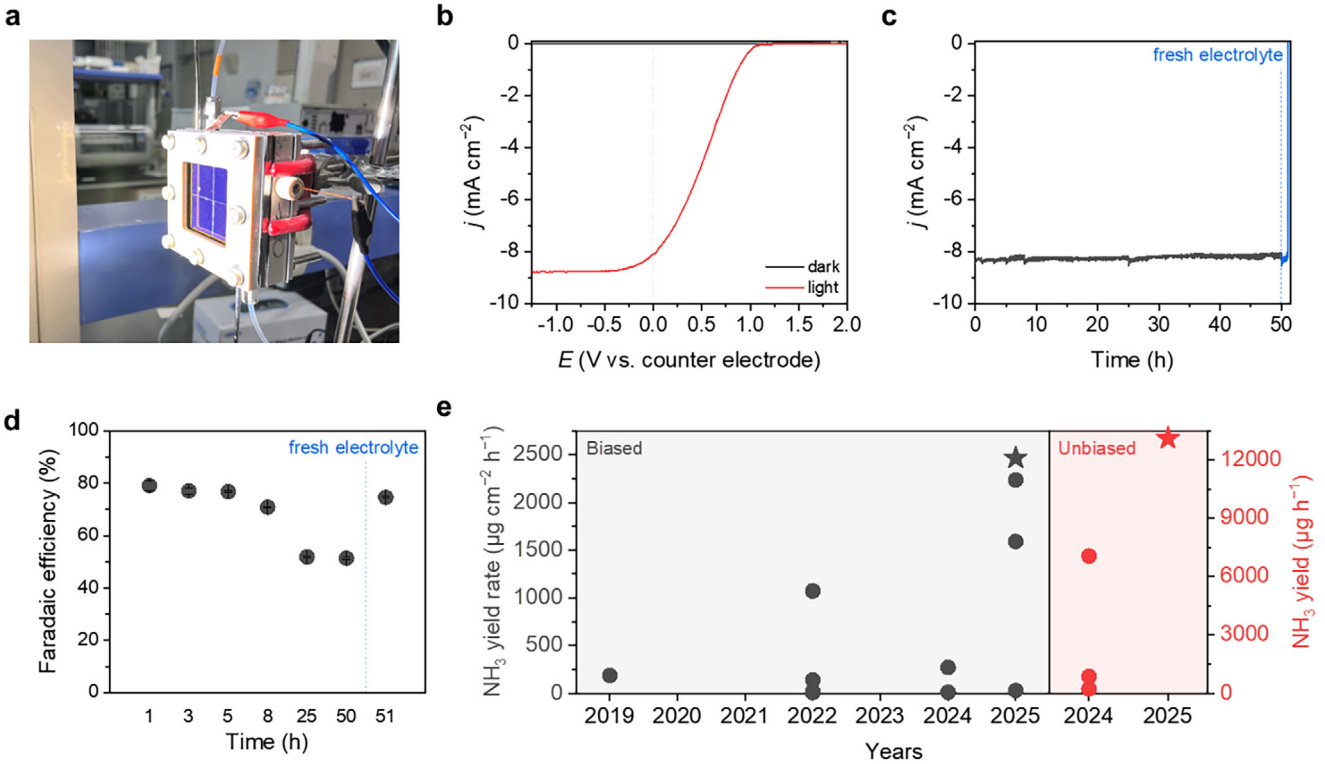

Figure 5. Scale-up system for the bias-free NO_3RR. a) Photograph of large-scale Ni/*c*-Si ABC 4 cells photocathode. b) LSV curves of the large-scale Ni/*c*-Si ABC 4 cell photocathode. c) Bias-free operating current in an integrated large-scale PEC system. d) Faradaic efficiency of the large-scale unassisted solar NH_3 production e) NH_3 production rate comparison with previously reported biased and unbiased PEC NO_3RR production system.

demonstrates the highest reported solar-to-ammonia yield (2468 μg cm^{-2} h^{-1}) among biased PEC NO_3RR systems. Additionally, it achieves not only the highest STA efficiency among unbiased systems but also the highest ammonia production yield (13850 μg h^{-1}), attributed to the successful scale-up of our system, further emphasizing its competitiveness and scalability for real-world applications.

3. Conclusion

A PEC NO_3RR achieving a high NH_3 production rate of 2468 μg cm^{-2} h^{-1} (at −0.1 V vs RHE) was realized using a Ni/*c*-Si ABC photocathode. This high performance was attributed to a self-activation process that transformed the Ni surface into $Ni(OH)_2$. This transformation suppressed the HER and enhanced the NO_3RR. Notably, this self-activation process was the most prevalent under alkaline conditions, a conclusion supported by the exclusive observation of $Ni(OH)_2$ crystalline structures on the Ni surface via HR-TEM analysis. Additionally, DFT calculations provided insights into the NO_3RR pathway on $Ni(OH)_2$ versus Ni surfaces, elucidating the superior catalytic activity of $Ni(OH)_2$ for the NO_3RR. Ultimately, this study led to the development of a bias-free and stable solar-to-NH_3 production system that achieved a high efficiency (STA = 3.8%, NH_3 Yield = 554 μg cm^{-2} h^{-1}) using a modularized *c*-Si ABC photocathode. This system represents the most efficient and highest-yielding PEC NO_3RR reported to date.

4. Experimental Section

Fabrication of Crystalline Silicon All-Back Contact (c-Si ABC) Solar Cell: A *p*-type Si wafer with a resistivity ranging from 1 to 3 Ω·cm and a thickness of 120 μm was used to fabricate the *c*-Si ABC solar cell. An interdigitated emitter and a back surface field (BSF) were fabricated on the backside of each cell through selective area diffusion of phosphorus and boron. Patterned SiO_2 diffusion barriers with thicknesses of 900 nm were used to enable elemental doping. Plasma-enhanced chemical vapor deposition (PE-CVD; PEH-600, SORONA) was used to deposit 900 nm-thick SiO_2 films on the front and rear sides of the Si substrate. To create a patterned diffusion barrier for the emitter contact, the SiO_2 film on the backside of the substrate was subjected to photolithography and SiO_2 etch-back processes using a diluted HF solution. Subsequently, a BSF layer was formed in a tube furnace at 880 °C, employing a boron dopant source (B155, Filmtronics) in a mixed atmosphere of N_2 (500 sccm). Except for the emitter and BSF regions, the entire surface was coated with a 10-nm thick Al_2O_3 layer at 200 °C via atomic layer deposition (Atomic premium, CN1), followed by the deposition of a 60 nm-thick SiN_X film at 350 °C using PE-CVD. For the metal electrodes, photolithography was employed to form interdigitated grid patterns at the emitter and BSF regions, followed by the thermal deposition of a 2 μm-thick Ag film.

Fabrication of c-Si ABC Solar Module: To facilitate the modularization process, a manufactured *c*-Si ABC unit cell was used. The glass substrate (Asahi Glass, AGC Inc.) was coated with a transparent ultraviolet (UV) curable polymer (NOA 63, Norland Products, Inc.). Multiple unit cells were arranged on a coated substrate for a series of connections. The assembly was then exposed to UV radiation for 15 min to ensure the complete curing of the polymer, resulting in the formation of a transparent handling substrate for the solar module. To establish the interconnections between the unit cells in series, an aluminum

(Al) contact electrode was created via thermal evaporation. An Al electrode was fabricated between the unit cells to enable efficient electrical coupling.

Characterization of c-Si ABC Solar Cell and c-Si Solar Module: The photovoltaic characteristics of the *c*-Si ABC solar cell and *c*-Si solar module were examined using a solar simulator (Oriel Sol3A, Newport) under standard air mass 1.5 global (AM 1.5 G) spectral conditions. The incident flux was quantified using a calibrated power meter and verified using a solar cell calibrated by the National Renewable Energy Laboratory (PV Measurements Inc.). To measure the external quantum efficiency, a xenon (Xe) light source and monochromator were utilized within a wavelength range of 300–1100 nm. This allowed for a precise evaluation of the response of the device to different light wavelengths.

Fabrication of c-Si ABC Photocathode: A copper wire was attached to the BSF region of the *c*-Si ABC unit or module cell, with a silver paste (Elcoat P-100, CANS). Next, a metal foil (electrocatalyst) was connected to a small portion of the emitter region using silver paste (Elcoat P-100, CANS), and covered the rest of the parts with tape(insulation layer) to avoid unnecessary contact. To further enhance stability, the Ni foil fully encapsulates the bottom surface of the photocathode, acting as an encapsulation layer that protects the device from direct electrolyte penetration while simultaneously serving as an efficient electrocatalyst for NO_3RR. Finally, the *c*-Si photoelectrode, except for the light-receiving area (4 cm^2) on the front side and the catalytic reaction area (4 cm^2) on the rear side, was covered with epoxy resin (JB Weld) to seal and fix the photocathode(Figure S13, Supporting Information).

Preparation of NiFe-LDH on Ni Foam: Previously published paper was reffered on the simple synthesis of NiFe-LDH at room temperature, which demonstrated high activity and stability. The NiFe-LDH used in this study was synthesized by immersing nickel foam in a 0.5 M $FeCl_3$ solution for 4 min. The characterization of the NiFe-LDH is shown in Figures S10 and S11 (Supporting Information).

Characterization of Ni Catalyst and NiFe LDH Anode: The *J-V* and *J-t* characteristics were recorded using a potentiostat (IviumStat, Ivium Technologies) under the illumination of an AM 1.5G solar simulator with an intensity of 100 mW cm^{-2}. Crystalline properties of Ni foil and NiFe-LDH were examined by XRD patterns using a Bruker AXS D8 Advance X-ray diffractometer equipped with Cu Kα radiation (λ = 1.5406 Å). Scans were taken between the 2θ range of 10° and 90° with a step size of 0.02°. Scanning electron microscopy (SEM) was performed using cold field-emission SEM on a Hitachi High-Technologies S-4800 instrument to confirm the morphology of NiFe-LDH. The accelerating voltage was set to 15 kV. The surface chemical and electronic states of the Ni electrodes before and after the CA tests were determined using X-ray photoelectron spectroscopy (XPS) with an Al K-Alpha source. A UV–vis spectrometer (UV-2600i, Shimadzu) was used for quantitative analysis of the NH_3 generated during the CA measurements.

(Photo) Electrochemical Measurements: The photoelectrochemical characteristics of the Ni/*c*-Si ABC photocathode were examined using a 450-watt xenon solar simulator (Oriel, Sol3A, Newport) with an AM 1.5G spectral calibration filter installed. Electrochemical measurements were conducted using a potentiostat electrochemical analyzer (nStat, Ivium Technologies) in a three-electrode and H-cell setup consisting of two chambers separated by a selemion anion exchange membrane (Nafion 117 proton exchange membrane in the neutral electrolyte). A Hg/HgO electrode (Ag/AgCl in the neutral electrolyte) and Pt wire served as the reference and counter electrodes, respectively. Electrolytes were used 1 M KOH solution (or 1 M PBS solution) containing 0.5 M KNO_3. Linear sweep voltammetry (LSV) was conducted at a scan rate of 10 mV s^{-1}. The LSV curve of the NiFe-LDH anode was shown as an inverted curve to distinguish it from the peroxidation peaks. Chronoamperometry (CA) was conducted at a constant potential −0.1 V (vs RHE) and at 0 V (vs counter electrode) under bias-free conditions for 1 h, and with no changes made to either the photocathode or the anode during the cycle test other than replacing with fresh electrolyte (1 M KOH with 0.5 M KNO_3) between cycles. All the potentials were converted to the RHE reference scale using the following equation:

$$E\,(vs.RHE) = E\,(vs.Hg/HgO) + 0.0592V \times pH + E_{Hg/HgO}\,(reference) = E\,(vs.Ag/AgCl) + 0.0592V \times pH + E_{Ag/AgCl}\,(reference) \quad (3)$$

$$\left(E_{Hg/HgO}\,(reference) = 0.118V vs.NHE at 25°C\right) \quad (4)$$

$$\left(E_{Ag/AgCl}\,(reference) = 0.195V vs.NHE at 25°C\right) \quad (5)$$

Indophenol Blue Method and Faradaic Efficiency Calculation: The indophenol blue method was used to quantify NH_3 during the CA measurements. After CA measurement, the samples were diluted to within the detectable range. Then, 1 mL of 1 M NaOH solution containing 5 wt.% salicylic acid and 5 wt.% Sodium citrate was mixed with 1 mL of the diluted sample. Next, 0.5 mL of 0.05 M NaOCl and 0.1 mL of 1 wt.% sodium nitroferricyanide solution were added. The blended solutions were mixed and aged for 1 h in the dark. Finally, the absorbance of the mixed sample was measured at 655 nm using a UV-vis spectrophotometer. A calibration curve obtained using a set of NH_4Cl solutions with known concentrations as standards was used to calculate the NH_3 concentration that was observed (Figure S5, Supporting Information). The Faradaic efficiency (FE) for NH_3 produced during the CA measurements was calculated using the following Equation (6): where n was 8 for the conversion of nitrate to NH_3, the number of electrons required to produce one NH_3 molecule, F was 96485 C mol^{-1}, and was the Faradaic constant.

$$Faradaic\ efficiency\ \ (\%) = \frac{n \times NH_3 concentration\ \ (mol\ L^{-1}) \times F\ (C\ mol^{-1}) \times volume of\ electrolyte\ \ (L)}{passed\ charge\ during\ rxn\ \ (C)} \times 100 \quad (6)$$

Isotope Tracing NH_3 ($^{15}NH_3$) Detection: To determine whether the produced NH_3 was contaminated by another N source, isotope tracing experiments were performed using $K^{15}NO_3$ (Sigma–Aldrich, 98 atom % ^{15}N) as the N source. Isotope tracing was conducted using proton nuclear magnetic resonance spectroscopy (H-NMR) (600 MHz FT-NMR, Bruker) to quantitatively analyze $^{15}NH_4^+$. When $K^{15}NO_3$ was converted to $^{15}NH_3$ photoelectrochemically, The samples obtained from the electrolyte after the PEC reaction were acidified to pH3 by adding 3 M HCl ($^{15}NH_4^+$). The samples were then mixed with 0.1 mL DMSO, and H-NMR spectra were obtained. Based on the calibration curves created from a set of $^{15}NH_4Cl$ (Sigma–Aldrich, 98 atom % ^{15}N) standard solutions, the $^{15}NH_4^+$ concentrations were determined. Isotope-tracing experiments with $K^{14}NO_3$ as the N source were performed using the same method.

Density Functional Theory (DFT) Calculational Methods: In this study, the DFT calculations were conducted using the Vienna ab initio simulation package (VASP).[58,59] The pseudopotentials were parameterized using the Perdew–Burke–Ernzerhof (PBE) method based on the projector–augmented–wave (PAW) method.[60,61] Exchange-correlation functionals were described with RPBE and PBE + U to calculate the reduction reactions on the Ni and $Ni(OH)_2$ surfaces, respectively.[62] The rotationally invariant formulation by Dudarev was used to apply the generalized gradient approximation (GGA) + U with the effective Hubbard U parameter U_{eff} = U–J = 5.5 eV for Ni atoms in $Ni(OH)_2$.[63] The catalytic reactions of the 4 × 4 Ni (111) and 2 × 1 $Ni(OH)_2$ (101) was calculated.[64] The 3 × 3 × 1 and 3 × 2 × 1 k-points were sampled in the Brillouin zone using the Monkhorst–Pack method.[65] The energy cutoff for the plane-wave basis was set to 400 eV, and the structures were optimized with a force criteria of 0.03 eV $Å^{-1}$. The vacuum height was 15 Å to avoid interactions between periodic cells, and the half-bottom layers were fixed during the optimization calculations to mimic the bulk property. The optimized structures of the Ni (111) and Ni(OH) (101) slabs are shown in Figure S14 (Supporting Information). The most energetically stable structure among all pos-

sible arrangements was determined for each reaction step, and through this systematic procedure, the whole multi-step reaction pathway was established. All the optimized structures from DFT calculations were drawn using VESTA.[66] The free energy, ΔG, was obtained from the following equation. $\Delta G = \Delta H + \Delta ZPE - T\Delta S$, where H, ZPE, T, and S represent the enthalpy, zero-point energy, temperature, and entropy, respectively. H was the total energy obtained from the DFT calculation, and the ZPE and ΔS values were adopted from the previous study.[67]

Supporting Information

Supporting Information is available from the Wiley Online Library or from the author.

Acknowledgements

W.J. and H.G. contributed equally to this work. The authors thank UNIST Central Research Facilities (UCRF) for the support of its facilities and equipment. This work was supported by the New Renewable Energy Core Technology Development Project of the Korea Institute of Energy Technology Evaluation and Planning (KETEP) granted financial resource from the Ministry of Trade, Industry & Energy, Republic of Korea (No. 20223030010240). This work was also supported by the National Research Foundation (NRF), funded by the Ministry of Science and ICT Planning [RS-2023-00222006]. This research was supported by Basic Research Program through the National Research Foundations of Korea (NRF) funded by the Ministry of Education (RS-2023-00248370). This work was supported by the National Institute of Supercomputing and Network/Korea Institute of Science and Technology Information with supercomputing resources including technical support KSC-2023-CRE-0552.

Conflict of Interest

The authors declare no conflict of interest.

Author Contributions

J.-W.J., K.S. proposed and directed the project. W.J. and H.G. conceived and designed the experiments. W.J. and J.P. fabricated solar cells, solar modules, and photocathodes. H.G., J.J., A.T., and J.M.Y. synthesized and characterized the Ni and NiFe-LDH catalysts and measured the photoelectrochemical performance of the photocathode. K.C., S.K. performed the DFT calculation. W.J., H.G., J.J., J.P., A.T., J.M.Y., K.C., J.-W.J., and K.S. co-wrote the manuscript. All authors contributed to the discussion and interpretation of the results.

Data Availability Statement

The data that support the findings of this study are available from the corresponding author upon reasonable request.

Keywords

crystalline silicon, density functional theory calculation, nickel hydroxide, photoelectrochemical, unassisted nitrate reduction

Received: April 7, 2025
Published online: June 23, 2025

[1] U. G. Survey, 2024.
[2] H. E. Kim, J. Kim, E. C. Ra, H. Zhang, Y. J. Jang, J. S. Lee, *Angew. Chem.* **2022**, *134*, 202204117.
[3] S. Choe, S. M. Kim, Y. Lee, J. Seok, J. Jung, J. S. Lee, Y. J. Jang, *Nano Convergence* **2021**, *8*, 22.
[4] D. R. MacFarlane, P. V. Cherepanov, J. Choi, B. H. Suryanto, R. Y. Hodgetts, J. M. Bakker, F. M. F. Vallana, A. N. Simonov, *Joule* **2020**, *4*, 1186.
[5] A. Kim, H. Kim, D. Lim, S. Cheon, H. Lim, *ACS Sustainable Chem. Eng.* **2023**, *11*, 155.
[6] R. Schlögl, in *Handbook of heterogeneous catalysis*, Wiley-VCH, Weinheim, Germany **2008**.
[7] M. Capdevila-Cortada, *Nat. Catal.* **2019**, *2*, 1055.
[8] D. Feng, L. Zhou, T. J. White, A. K. Cheetham, T. Ma, F. Wei, *Nano-Micro Lett.* **2023**, *15*, 203.
[9] Y. J. Jang, T. A. Evans, B. Samanta, K. Zeng, M. C. Toroker, K.-S. Choi, *J. Mater. Chem. A* **2021**, *9*, 20453.
[10] Y. Wang, Y. Yu, R. Jia, C. Zhang, B. Zhang, *Natl. Sci. Rev.* **2019**, *6*, 730.
[11] P. H. van Langevelde, I. Katsounaros, M. T. Koper, *Joule* **2021**, *5*, 290.
[12] D. Majumdar, N. Gupta, *Indian journal of environmental health* **2000**, *42*, 28.
[13] Y. Wang, C. Wang, M. Li, Y. Yu, B. Zhang, *Chem. Soc. Rev.* **2021**, *50*, 6720.
[14] Y. Wang, A. Xu, Z. Wang, L. Huang, J. Li, F. Li, J. Wicks, M. Luo, D.-H. Nam, C.-S. Tan, *J. Am. Chem. Soc.* **2020**, *142*, 5702.
[15] F. Wang, Q. Ding, J. Ding, Y. Bai, H. Bai, W. Fan, *Chem. Eng. J.* **2022**, *450*, 138260.
[16] S. Ren, R.-T. Gao, N. T. Nguyen, L. Wang, *Angew. Chem., Int. Ed.* **2024**, *63*, 202317414.
[17] J. Ding, Y. Lyu, H. Zhou, B. Johannessen, X. Zhang, J. Zheng, S. P. Jiang, S. Wang, *Applied Catalysis B: Environment and Energy* **2024**, *345*, 123735.
[18] Z. Luo, T. Wang, J. Gong, *Chem. Soc. Rev.* **2019**, *48*, 2158.
[19] W. Zheng, L. Zhu, Z. Yan, Z. Lin, Z. Lei, Y. Zhang, H. Xu, Z. Dang, C. Wei, C. Feng, *Environ. Sci. Technol.* **2021**, *55*, 13231.
[20] J. Zheng, Y. Lyu, C. Xie, R. Wang, L. Tao, H. Wu, H. Zhou, S. Jiang, S. Wang, *Adv. Mater.* **2018**, *30*, 1801773.
[21] J. Zheng, Y. Lyu, R. Wang, C. Xie, H. Zhou, S. P. Jiang, S. Wang, *Nat. Commun.* **2018**, *9*, 3572.
[22] G. Huang, R. Fan, X. Zhou, Z. Xu, W. Zhou, W. Dong, M. Shen, *Chem. Commun.* **2019**, *55*, 377.
[23] B. Guo, A. Batool, G. Xie, R. Boddula, L. Tian, S. U. Jan, J. R. Gong, *Nano Lett.* **2018**, *18*, 1516.
[24] W. Jin, C. Shin, S. Lim, K. Lee, J. M. Yu, K. Seo, J.-W. Jang, *Appl. Catal., B* **2023**, *322*, 122086.
[25] H. Li, B. Liu, S. Feng, H. Li, T. Wang, J. Gong, *J. Mater. Chem. A* **2020**, *8*, 224.
[26] S. Wang, T. Wang, B. Liu, H. Li, S. Feng, J. Gong, *Natl. Sci. Rev.* **2021**, *8*, nwaa293.
[27] E. L. Warren, J. R. McKone, H. A. Atwater, H. B. Gray, N. S. Lewis, *Energy Environ. Sci.* **2012**, *5*, 9653.
[28] R. Fan, W. Dong, L. Fang, F. Zheng, M. Shen, *J. Mater. Chem. A* **2017**, *5*, 18744.
[29] B. Wu, T. Wang, B. Liu, H. Li, Y. Wang, S. Wang, L. Zhang, S. Jiang, C. Pei, J. Gong, *Nat. Commun.* **2022**, *13*, 4460.
[30] W. Jin, Y. Lee, C. Shin, J. Park, J. W. Jang, K. Seo, *Adv. Mater. Interfaces* **2024**, *11*, 2400178.
[31] R. Zhang, Y. Guo, S. Zhang, D. Chen, Y. Zhao, Z. Huang, L. Ma, P. Li, Q. Yang, G. Liang, *Adv. Energy Mater.* **2022**, *12*, 2103872.
[32] S. Han, H. Li, T. Li, F. Chen, R. Yang, Y. Yu, B. Zhang, *Nat. Catal.* **2023**, *6*, 402.
[33] A. Tayyebi, R. Mehrotra, M. A. Mubarok, J. Kim, M. Zafari, M. Tayebi, D. Oh, S.-h. Lee, J. E. Matthews, S.-W. Lee, *Nat. Catal.* **2024**, *7*, 510.

[34] T.-Y. Jeon, S. K. Kim, N. Pinna, A. Sharma, J. Park, S. Y. Lee, H. C. Lee, S.-W. Kang, H.-K. Lee, H. H. Lee, *Chem. Mater.* **2016**, *28*, 1879.
[35] Q. Yao, J. Chen, S. Xiao, Y. Zhang, X. Zhou, *ACS Appl. Mater. Interfaces* **2021**, *13*, 30458.
[36] C.-H. Chiang, Y.-T. Kao, P.-H. Wu, T.-R. Liu, J.-W. Lin, P.-T. Chen, J.-W. Lin, S.-C. Yang, H.-L. Chen, S. B. Patil, *J. Mater. Chem. A* **2023**, *11*, 11179.
[37] D. Lim, S. Kim, N. Kim, E. Oh, S. E. Shim, S.-H. Baeck, *ACS Sustainable Chem. Eng.* **2020**, *8*, 4431.
[38] B. Zhan, C. Liu, H. Chen, H. Shi, L. Wang, P. Chen, W. Huang, X. Dong, *Nanoscale* **2014**, *6*, 7424.
[39] L. Xia, Y. Liao, Y. Qing, H. Xu, Z. Gao, W. Li, Y. Wu, *ACS Appl. Energy Mater.* **2020**, *3*, 2996.
[40] J. Potočnik, M. Novaković, M. Perović, M. Bošković, N. Bundaleski, M. Popović, *Vacuum* **2024**, *230*, 113619.
[41] J. Potočnik, M. Novaković, M. Popović, *Optical Materials* **2024**, *154*, 115665.
[42] J. Zhou, M. Wen, R. Huang, Q. Wu, Y. Luo, Y. Tian, G. Wei, Y. Fu, *Energy Environ. Sci.* **2023**, *16*, 2611.
[43] J. D. Butson, A. Sharma, H. Chen, Y. Wang, Y. Lee, P. Varadhan, M. N. Tsampas, C. Zhao, A. Tricoli, H. H. Tan, C. Jagadish, S. Karuturi, *Adv. Energy Mater.* **2022**, *12*, 2102752.
[44] M. Gong, Y. Li, H. Wang, Y. Liang, J. Z. Wu, J. Zhou, J. Wang, T. Regier, F. Wei, H. Dai, *J. Am. Chem. Soc.* **2013**, *135*, 8452.
[45] J. M. Yu, J. Song, Y. K. Kim, J. Oh, K. Y. Kim, W. Y. Noh, W. J. Byun, J. U. Lee, C. Yang, J.-W. Jang, *Nano Lett.* **2023**, *23*, 5092.
[46] X. Li, C. Liu, Z. Fang, L. Xu, C. Lu, W. Hou, *Small* **2022**, *18*, 2104354.
[47] C. Ballif, F.-J. Haug, M. Boccard, P. J. Verlinden, G. Hahn, *Nat. Rev. Mater.* **2022**, *7*, 597.
[48] K. Jia, Y. Bai, X. Wang, L. Yang, P. Yang, H. Bai, G. Xu, W. Fan, *Inorg. Chem.* **2025**, *64*, 3959.
[49] W. J. Dong, J. P. Menzel, Z. Ye, Z. Long, I. A. Navid, V. S. Batista, Z. Mi, *Small* **2025**, *21*, 2412089.
[50] A. Tayyebi, J. Juyeon, M. H. Moghaddam, M. Zafari, H. -j. Go, D. Lee, M. Tayebi, H.-Y. Yang, C. Shin, M. del Carmen Gimenez-Lopez, *EES Catalysis* **2025**, *3*, 446.
[51] H. E. Kim, D. H. Wi, J. S. Lee, K.-S. Choi, *ACS Energy Lett.* **2024**, *9*, 1993.
[52] M. Xu, F. Xu, K. Zhu, X. Xu, P. Deng, W. Wu, W. Ye, Z. Sun, P. Gao, *Composites Communications* **2022**, *29*, 101037.
[53] S. Zhou, K. Sun, C. Y. Toe, J. Yin, J. Huang, Y. Zeng, D. Zhang, W. Chen, O. F. Mohammed, X. Hao, *Adv. Mater.* **2022**, *34*, 2201670.
[54] F. Wang, Q. Ding, Y. Bai, H. Bai, S. Wang, W. Fan, *Inorg. Chem. Front.* **2022**, *9*, 805.
[55] J. M. Walls, J. S. Sagu, K. U. Wijayantha, *RSC Adv.* **2019**, *9*, 6387.
[56] C. Han, C. Li, J. A. Yuwono, Z. Liu, K. Sun, K. Wang, G. He, J. Huang, P. V. Kumar, J. Vongsvivut, *Energy Environ. Sci.* **2024**, *17*, 5653.
[57] S. Ren, R. T. Gao, J. Yu, Y. Yang, X. Liu, L. Wu, L. Wang, *Angew. Chem., Int. Ed.* **2024**, *63*, 202409693.
[58] G. Kresse, J. Furthmüller, *Comput. Mater. Sci.* **1996**, *6*, 15.
[59] G. Kresse, J. Furthmüller, *Phys. Rev. B* **1996**, *54*, 11169.
[60] P. E. Blöchl, *Phys. Rev. B* **1994**, *50*, 17953.
[61] J. P. Perdew, K. Burke, M. Ernzerhof, *Phys. Rev. Lett.* **1996**, *77*, 3865.
[62] A. Liechtenstein, V. I. Anisimov, J. Zaanen, *Phys. Rev. B* **1995**, *52*, R5467.
[63] S. L. Dudarev, G. A. Botton, S. Y. Savrasov, C. Humphreys, A. P. Sutton, *Phys. Rev. B* **1998**, *57*, 1505.
[64] Y. Tang, L. Dong, H. B. Wu, X.-Y. Yu, *J. Mater. Chem. A* **2021**, *9*, 1456.
[65] H. J. Monkhorst, J. D. Pack, *Phys. Rev. B* **1976**, *13*, 5188.
[66] K. Momma, F. Izumi, *J. Appl. Crystallogr.* **2008**, *41*, 653.
[67] F. Ai, J. Wang, *ACS Omega* **2022**, *7*, 31309.